communications earth & environment

A Nature Portfolio journal

Article

https://doi.org/10.1038/s43247-025-02872-3

Novel pathway of chalcopyrite formation at low temperature in microenvironments of acidic, metal-rich sediments

Andrey M. Ilin[1,13], Iñaki Yusta[1], Maxim Ilyn[2], Ana Martinez-Amesti[3], Charlotte van der Graaf[4], Irene Sánchez-Andrea[5], Andreas Scheinost[6], Damien Prieur[6,7], Andrea Sorrentino[8], Robert Oliete[8], Zhiquan Li[9], Weiduo Hao[10], Yuhao Li[11], Daniel Alessi[11], Kurt O. Konhauser[11] & Javier Sánchez-España[12]

Chalcopyrite ($CuFeS_2$) is the main source of copper worldwide and is usually formed at high temperature. Its occurrence at low temperature is poorly documented, and the mechanisms controlling its formation remain uncertain. We found evidences of chalcopyrite formation in acidic pit lake sediments at ~ 12 °C. Using high-resolution electron microscopy and synchrotron-based spectroscopy, we observed aggregates of nanoscale crystals with the composition and structure of disordered chalcopyrite. Laboratory incubations at 20 °C and geochemical modelling suggest that microbial activity may contribute to chalcopyrite formation under these conditions. Particularly, crystal growth was associated with hollow structures resembling microbial cell surfaces, and on the membranes of eukaryotic-like cells, providing nucleation sites. Our findings suggest that microbial processes, including the production of hydrogen sulfide and the presence of organic surfaces, promote chalcopyrite formation at low temperature. This has implications for understanding copper and sulfur cycling and its potential biotechnological application in sulfidic environments.

Chalcopyrite is one of the most abundant copper (Cu)- and iron (Fe)-bearing minerals and serves as the principal ore mineral for the global copper mining industry[1]. It is usually associated with high-temperature magmatic and hydrothermal systems, contributing to various types of mineral deposits such as porphyry Cu, epithermal, volcanogenic massive sulfides, sedimentary exhalative (SEDEX) or Mississippi Valley type deposits[2–7]. In all these systems, chalcopyrite is usually formed at moderate to high temperatures (>100 °C), which is consistent with its precipitation in experimental studies. For instance, the formation of chalcopyrite and bornite through sulfidation of hematite was reported under hydrothermal conditions between 200 and 300 °C[8]. A modern example of chalcopyrite formation can be found along the Mid-Atlantic Ridge, where nanometer-sized spheroids of chalcopyrite have been observed around hydrothermal vents[9]. In this deep-sea environment, anoxic brines (~350 °C) mix with cold oxic bottom seawater, promoting the precipitation of metal sulfides[9]. Although pyrite (FeS_2) nanoparticles (<100 nm) dominate the particulate matter emitted from these vents, precipitation of sphalerite [(Zn,Fe)S] and chalcopyrite has also been identified[9].

The formation of chalcopyrite at low temperature is rare in nature and is generally considered to be restricted to early diagenesis in sedimentary environments[10]. Direct precipitation of chalcopyrite at low temperature has been generally considered unlikely due to thermodynamic constraints, high activation energy, or kinetic barriers[10]. The formation of chalcopyrite has been experimentally demonstrated in acidic aqueous solutions (pH 2.0–4.5) at low temperature (<100 °C), where it forms through the transformation of preexisting Fe monosulfides, such as pyrrhotite ($Fe_{(1-x)}S$), in the presence of Cu-bearing salts[10]. The accepted mechanism for low-temperature chalcopyrite formation requires a pyrrhotite precursor that progressively incorporates Cu(II) cations, leading to a sequence of metastable Cu–Fe sulfide intermediates, and eventually chalcopyrite. In nature, chalcopyrite has been suggested to precipitate at low temperature in the form of aggregates composed of individual chalcopyrite nanoparticles (<10 nm) in riverbeds of the Clark Fork River in the US, which has been contaminated by mining and smelting activities from the Butte/Anaconda region[11]. Nonetheless, that study could not definitely confirm the authigenic origin of this chalcopyrite. Hence a detrital source, for instance transported downstream from the mining area, could not be ruled out.

More recently, the biogenic and abiotic precipitation of Cu–Fe sulfide nanoparticles, both in the presence and absence of the sulfate-reducing bacterium (SRB) *Desulfovibrio vulgaris*, was reported in an anoxic medium

A full list of affiliations appears at the end of the paper. e-mail: andrey.ilin@ehu.eus

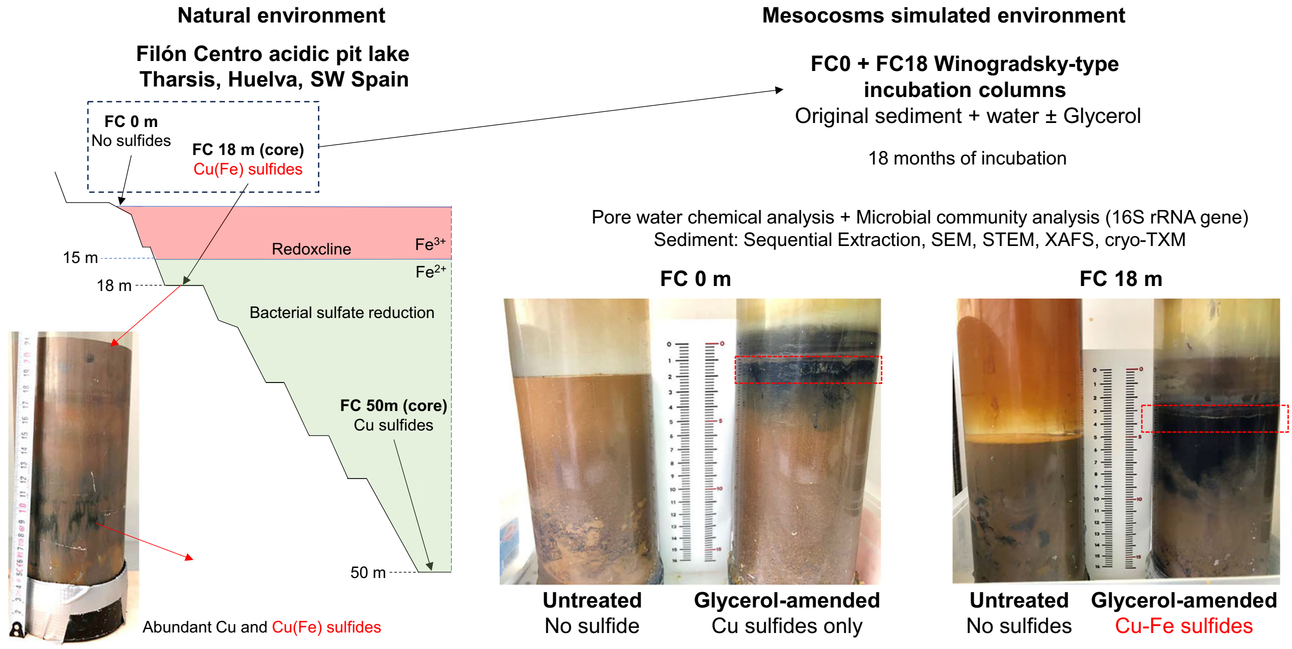

Fig. 1 | Summary of the studied samples and localization of the Cu–Fe sulfides in the Filón Centro (FC) APL (Tharsis, Huelva, Spain) and in the incubation columns built with the sediment and water from different depths of the APL. Red rectangle: sampled area selected for electron microscopy studies. Additional results are shown in Supplementary Figs. 1 and 2.

at 30 °C and pH 7.2[12]. The ratio of dissolved Fe(II) and Cu(II) cations largely determined the resulting mineral product, with chalcopyrite precipitating in media with Cu:Fe molar ratios of 1:1 or 1:2. Contrary to the mechanism proposed by Cowper et al. (1989)[10], Mansor et al. (2019)[12] suggested an inverse formation mechanism, where Fe(II) cations were incorporated into a precursor covellite (CuS) mineral phase to form chalcopyrite. Additionally, SRB accelerated the atomic rearrangement during the transformation of precursor sulfides into a Fe–Cu mixed phase. The authors also hypothesized that microenvironments around bacterial cells, possibly more acidic than the bulk surrounding, might promote mineral precipitation. However, the formation of these mixed Cu–Fe sulfides was not assessed at low pH, and studying the exact role of bacterial cells (whether active or passive) in the process was out of the scope of the experiment.

Authigenic Cu sulfides have been reported in the water column of acidic pit lakes (APL) and are considered to be a secondary mineral product of bacterial sulfate reduction (BSR), driven by the interaction of bacteriogenic hydrogen sulfide (H_2S) with Cu(II) cations[13–15]. However, these sulfides are typically composed of covellite, and the formation of chalcopyrite has never been observed as a result of BSR in acid mine drainage (AMD) systems.

In this work, we document, for the first time, the formation of chalcopyrite at low pH (pH 3.7–4.2), under mildly reducing conditions (ORP ~ 120 mV) and ambient temperature (20 °C) in sediments of an APL in southwest Spain (Supplementary Fig. 1) and reproduce the process in glycerol amended incubation columns that enhanced bacterial sulfate reduction (Supplementary Fig. 2). Crystals and framboids of chalcopyrite have been detected by a combination of scanning (SEM) and scanning transmission electron microscopy (STEM), X-ray absorption spectroscopy (XAS) and cryo-transmission X-ray microscopy (TXM). These chalcopyrite crystals were consistently nanometer-sized and were observed freely and in close spatial association with microbial cells. The conclusions emerging from our study offer new insights into possible formation pathways and raise the hypothesis that biological processes, whether directly or indirectly, may facilitate chalcopyrite crystallization under low-temperature and acidic conditions.

Results

Scanning and transmission electron microscopy

Copper sulfides were abundantly detected in anoxic sediments obtained from 18 m depth of Filón Centro APL (Fig. 1). These sediments were predominantly composed of schwertmannite ($Fe_{16}O_{16}(OH)_{9.6}(SO_4)_{3.2}\cdot 10H_2O$), jarosite ($(K,H_3O)Fe_3(OH)_6(SO_4)_2$) and goethite (FeOOH) giving them a characteristic brownish color. In the sediment core, intercalated dark layers appeared at 10–12 cm below the water/sediment interface and exhibited considerably higher Cu concentrations, as indicated by semi-quantitative X-ray fluorescence (XRF) analyses, compared to the rest of the sediment column (Fig. 1; *data not shown*). In the columns incubated in the laboratory, similar dark layers developed close to the water-sediment interface, corresponding to areas of acidity consumption and more reducing conditions, where the highest abundance of metal sulfides was observed[16]. Based on these observations, sediment color was used as a criterion for targeted sampling aimed at metal sulfide characterization.

In the sediment core, copper sulfides commonly appeared as clusters of nanometer-sized crystals composed exclusively of Cu and S, as confirmed by SEM coupled with energy dispersive X-ray spectroscopy (EDX) (Fig. 2A). Notably, some crystals also showed the presence of Fe in the mineral stoichiometry, forming an outer rim around the copper sulfide crystals (Fig. 2B–D). The micron-scale longitudinal profile of the elemental map revealed an inverse distribution trend for Cu and Fe, with the molar ratio approaching 1:1 towards the crystal edges. This chemical feature apparently defines a reaction front of Cu–Fe substitution within the crystal lattice (Fig. 2E).

The finding of Cu–Fe substitution within the copper sulfide crystals prompted further investigation into the mineral neoformation process. To simulate the natural conditions in the lake sediments, incubation columns (IC) were constructed using water and sediments from the APL, supplemented with glycerol as carbon source to stimulate bacterial sulfate reduction (Fig. 1; Supplementary Fig. 2)[16]. In these mesocosms, mixed Fe–Cu sulfides (i.e., no CuS) were exclusively found in the sediment samples from the glycerol-amended IC built with the material collected at 18 m depth from Filón Centro. These mixed sulfides were further analyzed by STEM (Fig. 3).

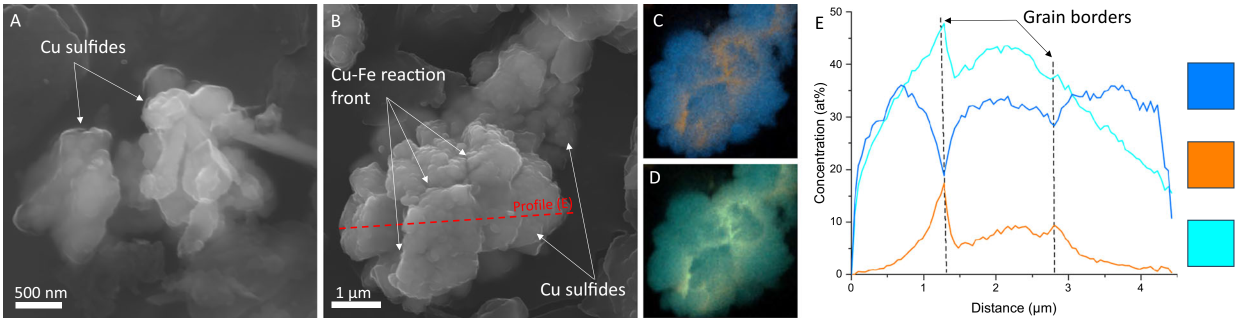

Fig. 2 | SEM micrographs of metal sulfide aggregates detected in the sediment core recovered from Filón Centro pit lake at a depth of 18 m. A Cluster of copper sulfide crystals. **B** Aggregate of copper sulfide crystals with the elemental maps of Fe + Cu (**C**) and Fe + S (**D**). **E** Longitudinal elemental profile along the line defined in (**B**) through the Cu-sulfide crystal (provided in atomic percent; at%).

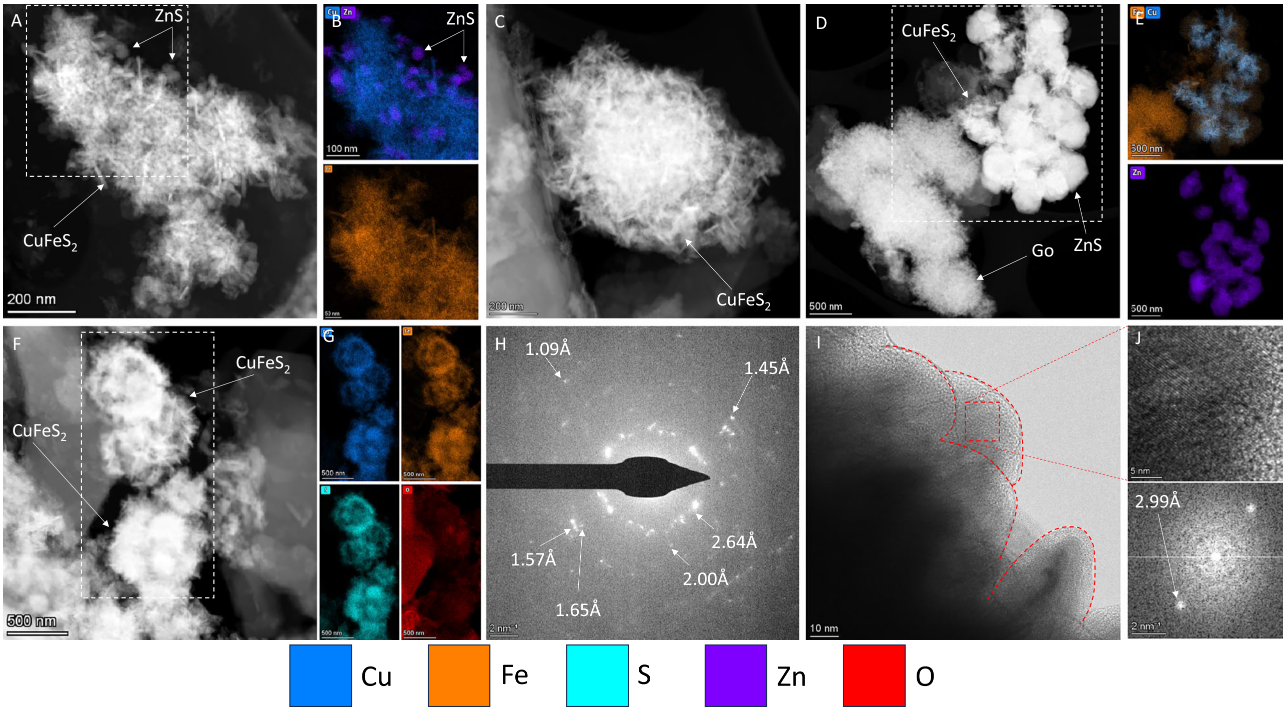

Fig. 3 | STEM micrographs of Cu–Fe sulfide aggregates detected in the glycerol-amended IC (built with material collected at 18 m depth) after 18 months of incubation (pH: 3.7; ORP: 123 mV; −1 cm depth in sediment layer). A, B Cluster of $CuFeS_2$ acicular crystals: HAADF and EDX elemental maps. **C** Sub-spherical aggregate of individual $CuFeS_2$ acicular crystals. **D, E** $CuFeS_2$ and ZnS aggregates and goethite spherical aggregates: HAADF and EDX elemental maps (Cu + Fe= gray). **F–J** Acicular $CuFeS_2$ crystals agglomerating around sub-spherical preexistent structure: HAADF, EDX elemental maps, SAED, HRTEM with amplified red area with lattice fringes and corresponding FFT.

Characteristic acicular nanosized crystals consistently showed the presence of S, Cu and Fe, with a clear overlap of its elemental maps (Fig. 3B, E, G). The STEM-EDX analyses displayed crystals with a rather homogeneous Cu:Fe molar ratio of ~0.89−1.17. The crystals were commonly observed in clusters of needle-like structures (with individual needle thickness of ~30 nm), which aggregated either irregularly (Fig. 3A) or in spherical forms (Fig. 3C, D, F). Some of these aggregates formed compact pincushion-like spheroids, whereas others were apparently hollow (Fig. 3G). The crystals radiated outward from a central spherical template of around 500 nm in diameter of probable microbial origin. Selected area electron diffraction (SAED) of these crystals showed ring patterns indicative of a polycrystalline nature. The measured d-spacings of 2.64, 2.31, 2.04-2.00, 1.88, 1.71−1.65, 1.56, 1.45, 1.17 and 1.09 Å (Fig. 3H; Supplementary Fig. 3A-C) are consistent with a chalcopyrite crystalline structure (ICSD: 00-037-0471). High-resolution TEM (HRTEM) analysis showed a decrease in crystallinity from the core towards the edges of the acicular crystals (Fig. 3I). The core of the crystallites showed the presence of lattice fringes with a d-spacing of 2.99 Å (Fig. 3J, Supplementary Fig. 3D-F), likely corresponding to the (112) plane of chalcopyrite (3.04 Å), the most intense reflection in the powder XRD.

X-ray absorption spectroscopy

The speciation and coordination chemistry of Cu atoms were analyzed by XAS in the sediment samples from the glycerol-amended FC18 and FC0 ICs. Relevant pure reference mineral samples were also analyzed for comparison. The XANES spectra of both samples showed the presence of a pre-edge feature at 8979 eV, being more marked in sample FC18, and a white-line position at 8986 eV, both in line with the pre-edge and white-line features of the references chalcopyrite and covellite with S-coordinated monovalent Cu (Fig. 4A)[17,18]. The k^3-weighted EXAFS spectra and the Fourier transform magnitudes (FTM) are shown in Fig. 4B. The fine structure of the samples from the ICs showed the prevalence of Cu–S species, as expected. We found remarkable similarities between the chalcopyrite reference and the sediment samples from the glycerol-amended FC18 IC

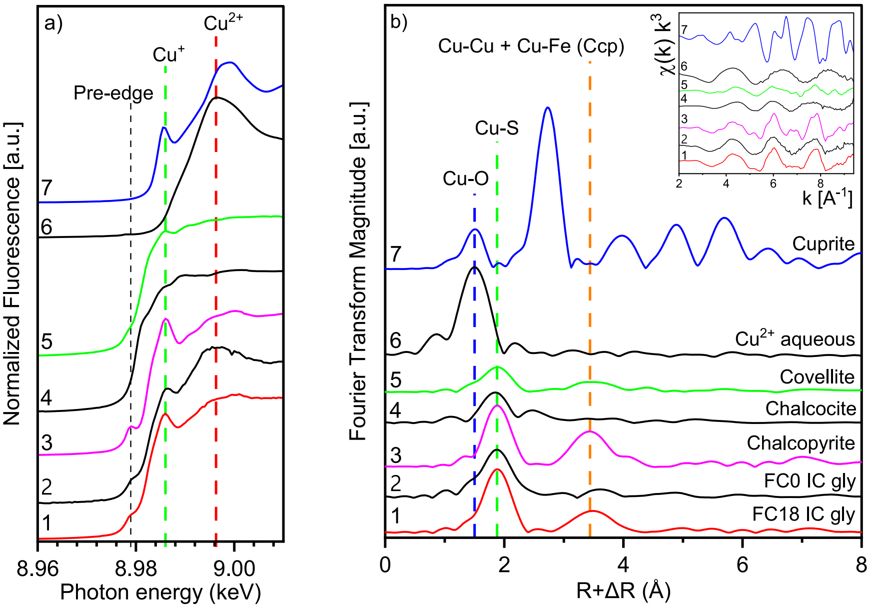

Fig. 4 | Copper K-edge XAS spectra of the two sediment samples and of selected Cu references. **a** XANES; **b** k^3-weighted chi (χ) function of the EXAFS spectra (inset) and corresponding Fourier transform magnitude (FTM). On XANES, the vertical black line shows the position of the pre-edge feature, the green line shows the white line position of sulfur-coordinated Cu(I) and the red shows the Cu(II). On the FTM, the vertical lines represent backscattering peaks of O-coordinated Cu (blue), S-coordinated Cu (green), and the nearest Cu and Fe atoms of chalcopyrite (orange). Ccp chalcopyrite.

considering especially the presence of the XANES pre-edge feature and also the second shell in FTM EXAFS at 3.4 Å (uncorrected for phase shift), which arises from backscattering of 4 Cu and 4 Fe atoms at 3.67 Å (Fig. 4)[19].

To derive the number of different Cu species in the sediment samples, their EXAFS spectra were analyzed by principal component analysis (PCA) using the iterative transformation factor analysis (ITFA) software package[20]. The Malinowski indicator values and the good reconstruction of the experimental data with 2 spectral components suggested that there are two main Cu-bearing mineral phases in the samples. Based on the VARIMAX loadings, component 1 prevailed in the sample from FC18 glycerol-amended IC and component 2 in the sample from FC0 glycerol-amended IC. As expected, the addition of the chalcopyrite reference did not increase the number of required components, hence chalcopyrite is indeed one of the components present in both sediment samples. We then tested several other references, including chalcocite and covellite as likely Cu sulfides. None of them provided a good spectral match of the sediment samples. We therefore isolated the endmember spectrum of the (unknown) second spectral component using ITFA following protocols[21,22]. Table 1 shows the structure of the two endmember components (chalcopyrite and the unknown component 2) as determined by EXAFS shell fitting in comparison to selected references based on coordination number (CN), distances to the neighboring atoms (R), and Debye-Waller parameters.

The chalcopyrite reference, identical to component 1 (Fig. 5A) as derived from the ITFA analysis of the sediment spectra, could be fitted with the nearest Cu–S at 2.30 Å, the nearest Cu–Cu and Cu–Fe shells at 3.73 Å, and another Cu–S shell at 4.36 Å, all distances 0.06 to 0.07 Å longer than given by the crystal structure data[19]. Note that EXAFS is not able to resolve the longer Cu–Fe path at 3.71 Å. The shell fit of component 2 provided a Cu–S distance of 2.31 Å and a Cu–Cu distance of 3.78 Å (Fig. 5B).

While component 1, which was found to have spectral features close to chalcopyrite, could be fitted correspondingly, component 2 was fitted with a Cu–S shell at 2.31 Å, and a Cu–Cu shell at 3.78 Å. Given that the distances of these two shells correspond largely to the structure of chalcocite, this phase is the most plausible candidate for the second Cu species present in the sediment. However, the two fitted shells also coincide with the two major shells in covellite (prevalently to the second Cu position[23]), while a closer Cu–Cu shell at 3.2 Å and a Cu–S shell at 3.56 Å could not be fitted. Hence although the match with chalcocite seems to be slightly better in terms of shell fit data, both the chalcocite and covellite references provided a rather poor spectral match with the sediment samples during the ITFA analysis. Consequently, component 2 is more consistently interpreted as an amorphous Cu(I) sulfide phase rather than a crystalline analog similar to one of the two crystalline references.

ITFA analysis also provided quantitative Cu speciation in FC18 and FC0 based on the two identified components. While Cu in FC0 consisted of 100 % of component 2, hence the amorphous Cu(I) sulfide, FC18 contained Cu of up to 39% as chalcopyrite, but still 61% as the precursor phase.

Cryo soft X-ray tomography and spectromicroscopy

Tomography at 520 eV and differential imaging at Fe and Cu L_3 edge/pre-edge energies were acquired from the sediment in glycerol-amended FC18 IC. The latter consists of acquiring images before and at the absorption edge energy of interest, particularly at Fe and Cu L_3 edges (Fig. 6B, D, respectively). Because the absorption of all the other elements is almost the same at these two energies, the differential image showed the Fe and Cu 2D distribution in the field of view (FOV). Few subspherical cells showed a differential contrast both at the Fe and Cu edges compatible with a shell-like Fe and Cu distribution (Fig. 6C, E). The Fe signal was distributed on the full cell but with a clear maximum of intensity at the border, where, due to the subspherical curvature, the Fe thickness was greater. For the same reason, Cu was detected just at the border: Cu signal was probably too weak to be detected everywhere on the cell but was detected in the region where X-rays cross the maximum Cu thickness, i.e., again at the border of the subspherical cell.

It must be pointed out that these 2D measurements cannot exclude the presence of Fe inside the cell. Nevertheless, the 3D volume reconstruction of the cell from tomography at 520 eV also supports the hypothesis of a shell-like distribution and co-localization of Fe and Cu. Indeed, in Fig. 6G where a central slice of the reconstructed volume is reported, a dense material is markedly visible all around the cell and in particular on the left side, as indicated by the arrow in Fig. 6G, single black spots could be clearly distinguished. Therefore, by combining the measurements from both differential imaging at Fe and Cu edges and tomography at 520 eV, a distribution of nanometric crystals (<100 nm) all over the cell membrane containing both Fe and Cu could be established. The nanocrystals' distribution was emphasized in red in the 3D rendering reported in Fig. 6H. The chemical specification of these objects was obtained by spectromicroscopy measures, extracting the full XAS from the corresponding pixels in the FOV. Spectrum from this Fe–Cu "coating" was reported (red line) and compared with other reference mineral spectra at both Fe and Cu L_3 edges in Fig. 6M, N, respectively. The resemblance with chalcopyrite reference spectra is very strong, allowing to identify as chalcopyrite the observed Fe- and Cu-rich cell

Table 1 | Cu K-edge EXAFS fit results of sediment samples from glycerol-amended FC18 IC (16 mo) and FC0 IC (16mo), in comparison to spectral components 1 and 2 derived from the sediment samples and a chalcopyrite reference, and other copper sulfide minerals

Sample	Path	CN[a]	*R* [Å][b]	σ^2 [Å^2][c]	ΔE_0 [eV][d]	*R* [%][e]	XRD-CN	XRD-R [Å]
FC18 IC (16 mo)	Cu–S$_1$	4.2	2.30	0.0059	7.1	4.6		
Gly-amended	Cu–Cu$_1$	6.8	3.75[f]	0.0150				
	Cu–Fe	2.5	3.75[f]	0.0099				
	Cu–S$_2$	5.0	4.30	0.0150				
FC0 IC (16 mo)	Cu–S$_1$	5.2	2.32	0.0103	7.3	9.2		
Gly-amended	Cu–Cu$_1$	2.6	3.76	0.0150				
(Component 2)	Cu–S$_1$	4.9	2.31	0.0094	7.2	8.0		
	Cu–Cu$_1$	4.5	3.78	0.0150				
Chalcopyrite	Cu–S$_1$	4.1	2.29	0.0035	9.6	5.6	4 S	2.26
($CuFeS_2$)	Cu–Cu$_1$	2.5	3.73[f]	0.0079			4 Cu	3.67
(Component 1)	Cu–Fe	5.3	3.73[f]	0.0067			4 Fe	3.67
	Cu–S$_2$	9.1	4.36	0.0103			12 S	4.30
Chalcocite	Cu–S$_1$	1.3	2.29	0.0020	8.4	4.1	3 S	2.31-2.36
(Cu_2S)	Cu–Cu$_1$	1.4	2.72	0.0079			7 Cu	2.66-3.03
Covellite	Cu–S$_1$	3.1	2.29	0.0105	11.6	10.2	3/4 S	2.19/2.31
(CuS)	Cu–Cu$_1$	1.0	3.16	0.0150			6/3 Cu	3.21/3.21
	Cu–S$_2$	4.1	3.58	0.0150			6/3 S	3.76/3.56
	Cu–Cu$_2$	3.0	3.77	0.0150			6/6 Cu	3.80/3.80

XRD coordination numbers and distances were derived from the crystallographic data for chalcopyrite[19], chalcocite[57] and covellite[23].

[a] CN: coordination number, error ± 25%.

[b] R: radial distance, error ± 0.01 Å.

[c] σ^2: Debye-Waller factor, error ± 0.002 Å^2.

[d] ΔE_0: shift in threshold energy.

[e] R: normalized least squares residual.

[f]: correlated Cu–Cu and Cu–Fe distances.

coating. Surely, Fe was detected also outside the cell (hot spot in Fig. 6C and "Gt" pink rendering indicated by an arrow in Fig. 6H, I). The corresponding XAS spectrum was reported in Fig. 6M (violet line) for comparison, and it showed a clearly different Fe oxidation state compared to the chalcopyrite. The presence of both Fe and Cu was detected around sub-spherical objects in the sample, resembling an organic structure (Fig. 6J–L). Notably, the spectral fingerprint of these precipitates was also comparable to the chalcopyrite (Fig. 6M, N).

Aqueous and sedimentary geochemistry and geochemical modeling

Geochemical analyses of the pore water after 18 months of incubation of the FC0 and FC18 IC samples indicated that the dissolved Fe concentration was considerably higher in the glycerol-amended IC compared to other ICs, while Cu was completely absent in the solutions (Supplementary Table 1). Analysis of the top sediment layer of the ICs following a sequential extraction protocol showed that S was preferentially associated with organic matter and secondary sulfides (step 6; Supplementary Table 2). The highest Fe concentrations were observed in the reducible fraction (step 4), which includes crystalline oxides with ferric iron like goethite and Fe(III)-containing hydroxysulfates like schwertmannite and jarosite. Apart from these fractions, Fe concentrations were notably high in the organic and secondary sulfide fraction in glycerol-amended FC18 ICs, generally <10% molar Fe (Supplementary Fig. 4). This Fe content is ascribed to the presence of poorly crystalline Cu±Fe sulfides, such as chalcopyrite, as described below.

The geochemical profiles obtained during the column incubation in the lab indicated that the pH values in the sediment pore waters of FC18 and FC0 were not drastically different (Supplementary Fig. 2)[16]. However, the evolution of pH in these profiles suggested that the activity of sulfate-reducing bacteria (SRB) was clearly more intense and extensive in FC18: in this column the maximum pH value (6.1) was reached after about 3 months of incubation. In contrast, FC0 reached its maximum pH (around 5.9) much later, at about 9 months, and only in a very narrow region. By 12 months, pH values were already declining, likely due to the consumption of the supplemented organic source.

Another factor that may play a crucial role in chalcopyrite formation is the presence of Cu sulfides in FC18 from the very beginning of the experiments, as observed in the original lake sediments (Fig. 2). These Cu sulfides were not detected in the shore sediments (FC0). This difference could be critical since the SRB activity in FC18 may have transformed the existing CuS precursors into chalcopyrite, whereas in FC0, the same microbial activity would have been spent first on forming those CuS precursors.

To better understand the controls on chalcopyrite formation in the studied systems, we calculated the saturation index of the pore waters with respect to different Cu- and Fe-containing sulfides under different chemical conditions (Fig. 7). When the concentrations of the reactants participating in Cu and Fe sulfide formation (i.e. Cu(II), Fe(II), SO_4^{2-} and H_2S), as well as the redox conditions (defined by the electronic potential, pe, being pe = Eh/59.2) and temperature remain constant, the calculations indicate that the pore waters in both FC18 and FC0 are strongly oversaturated with respect to chalcopyrite, covellite, and pyrite across the pH range of 1.0–8.0. In contrast, the iron monosulfides, such as mackinawite (FeS) and amorphous FeS, consistently showed undersaturation (Fig. 7A).

These calculations were based on a concentration of H_2S of 10 mg/L (as measured in acidic pit lake waters[13]) and a temperature of 25 °C. At a constant pH of 4.0 - reflecting conditions measured in the porewater of sediments in FC18 IC—the calculations showed a clear oversaturation with respect to covellite, chalcopyrite, and pyrite, even with minimal concentrations of Cu(II) and S^{2-} in the system. In contrast, FeS consistently exhibited undersaturation at all concentrations (Fig. 7B, C). However, when considering total S instead of S^{2-}, PHREEQC calculates the different S species

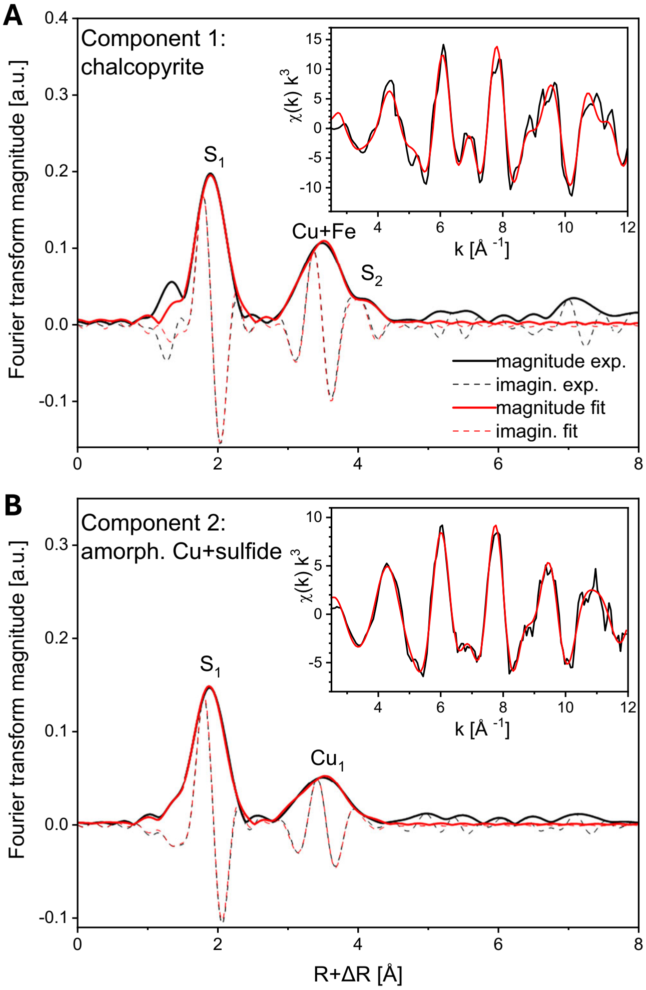

Fig. 5 | Experimental EXAFS spectra of the main components derived for FC18 and FC0 glycerol-amended IC sediment samples (black traces) and their reproduction by shell fitting (red traces). The plots (Component 1 (**A**) and Component 2 (**B**)) show the Fourier transform magnitude (bold lines) and the imaginary part (dashed lines); the insets show the corresponding k^3-weighted χ(k) spectra.

based on the pe value. We considered a pe window of 0–5 (equivalent to Eh of 0-300 mV, which is usually measured in BSR zones in AMD systems[13–15,24]. At low pe values (1–2, i.e., more reducing conditions), the program calculates (based on the activity coefficients included in the thermodynamic database) that at certain quantity of S^{2-}, as pe increases, the sulfide concentration decreases until it is virtually absent at pe=4.5 (where 99.99% of total S is in the form of sulfate, SO$_4^{2-}$). Under these conditions, chalcopyrite and covellite precipitation is theoretically possible (high SI values) as long as a minimal trace of S^{2-} is available, along with excess Cu(II) and Fe(II). However, as the S^{2-} concentration decreases (e.g., from 10^{-10} to 10^{-15} molar S^{2-}), the aqueous system becomes clearly undersaturated (very negative SI values), making the precipitation of these two minerals thermodynamically unfeasible (Fig. 7D, E).

If the concentrations of S^{2-}, Cu(II) and Fe(II), and pH, are kept constant, and Cu is introduced in the model as total Cu to assess the effect of the reducing conditions on the theoretical distribution of Cu species and on the saturation state of the investigated minerals, then the calculations show that at low pe values (<4), dissolved Cu may exist not only as Cu(II) cations but also as Cu(I) cations, and even as metallic copper (Cu[0]). This observation is important because the presence of Cu(I) cations in the aqueous system allows the formation of additional Cu(I)-bearing phases, such as chalcocite (Cu_2S), djurleite ($Cu_{31}S_{16}$) or anilite (Cu_7S_4), all of which show a strong theoretical oversaturation under the given chemical conditions (SI = 20–23; Fig. 7F). The saturation indexes of these more reduced Cu(I)-containing minerals are even higher than those of Cu(II)-containing minerals like covellite (SI = 12–13) (Cu oxidation state is discussed below). This suggests that the formation of these reduced minerals would be thermodynamically more favorable under the studied conditions (Fig. 7F). This is further supported by the Eh-pH plot in Fig. 8[25], where the analyzed pore waters (considered to be the parent solutions of these sulfides) plot near the boundary between the stability fields of Cu_2S and Cu[0]. Metallic Cu has also been detected by XAS in columns incubated with sediment from other pit lakes[26], which is in good agreement with the distribution of Eh-pH values in Fig. 8.

Discussion

Mineralogical, micro-textural and microbiological considerations

To the best of our knowledge, the detection of Cu–Fe sulfides in the dark sediment layers at 18 m depth of FC APL represents the first reported case of copper sulfides transforming into Cu–Fe sulfides in the natural environment as shown in Fig. 2. Moreover, it empirically supports the hypothesis that Cu sulfides can evolve into Cu–Fe sulfides, rather than starting from an Fe sulfide precursor – a topic that has been debated in the existing scientific literature[10,12].

Electron microscopy confirmed a close association between Cu and Fe in the sulfides detected both in the deep sediment and the incubation column experiments (Figs. 2–3). The complete overlap of the STEM-EDX elemental maps for Cu, Fe and S suggests the formation of mixed Cu–Fe sulfide acicular crystals. These nanosized crystals either lacked a specific orientation or aggregated into spherical, seemingly hollow structures. The Cu:Fe molar ratio, ranging from 0.89–1.17, as determined by STEM-EDX, correlates well with the precipitation of chalcopyrite ($CuFeS_2$). The Cu:S molar ratio of 0.48-0.54 further supports the presence of chalcopyrite over other possible minerals like bornite which might also be expected to precipitate under similar conditions (Fig. 8). SAED of these aggregates revealed a polycrystalline mineral phase, with d-spacings consistent with chalcopyrite. HRTEM identified lattice fringes with a d-spacing very close to 3.04 Å, corresponding to the strongest reflection of chalcopyrite in the XRD.

XAS results suggest that the precursor phase represented by the component 2 of PCA and sediment from FC0 glycerol-amended IC is a Cu sulfide with 4.9 S atoms at 2.31 Å and 4.5 Cu atoms at 3.78 Å. On the other hand, sediment from FC18 glycerol-amended IC can be considered as either a more disordered, Fe-poor chalcopyrite, or a mix of 39% of chalcopyrite and still 61% of the precursor phase.

Abundant nanosized mixed Cu–Fe crystals, closely related to subspherical cells in the cryogenized sediment sample from the glycerol-amended IC, suggest involvement of microbe-mineral interactions in their formation (Fig. 6). The Fe and Cu L_3 XANES spectral features of these Cu–Fe crystals closely matched the reference spectrum for chalcopyrite and were consistent with previously reported soft XANES spectra of chalcopyrite cleaved in vacuum[18,27,28].

The results of the cryo-TXM further support the precipitation of chalcopyrite in this low-temperature environment (Fig. 6) growing directly around a cell, whose nature (prokaryotic or eukaryotic) could not be clearly identified. Unlike the cryogenized sample, the sample analyzed by conventional STEM was not subjected to a specific treatment to preserve biological structures (e.g., HMDS protocol), hence any existing microbial cells were not conserved and likely exploded (collapsed) under the vacuum of the microscope. The subspherical cells observed under cryo-TXM appeared with smaller crystals and incomplete crust formation, which would likely represent an early stage of chalcopyrite coating (Fig. 3F).

The precipitation of chalcopyrite in the studied pit lake sediments aligns with the pathway proposed by Mansor et al.[12], which involves the formation of pure copper sulfide (likely an amorphous Cu sulfide, as was evidenced by XAS) followed by incorporation of Fe^{2+} from an Fe-rich solution. The abundance of Cu sulfides coming from the SRB activity in the water column and sediments of the initial core extracted from 18 m depth

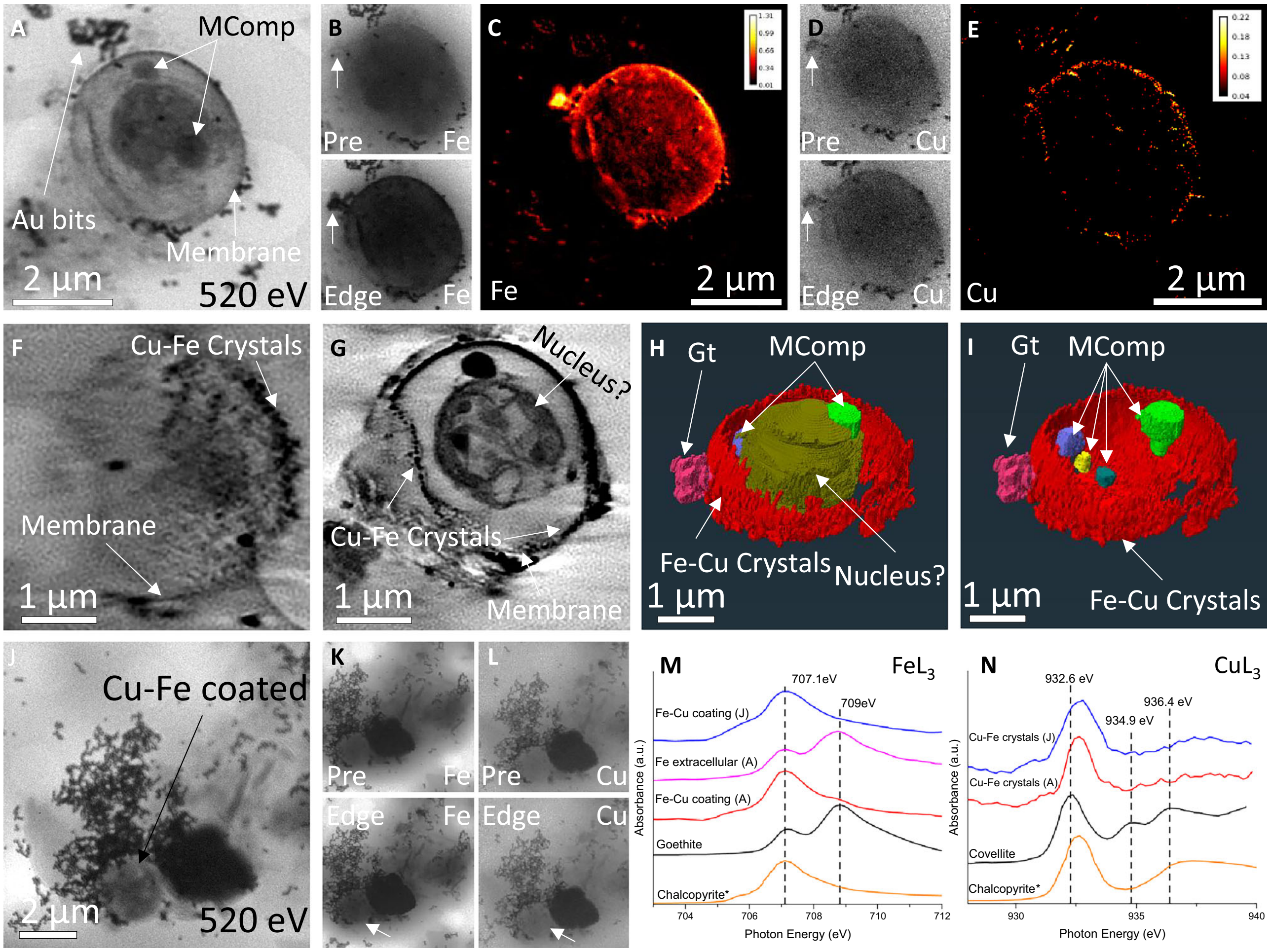

Fig. 6 | Transmission energy-filtered X-ray microscopy micrographs of cryo-genized sediment sample from glycerol-amended FC18 IC. A Sub-spherical cell coated with nanometric Cu–Fe crystals, including tomography slice acquired at the water window (520 eV). **B, C** Transmission images acquired at Fe pre-edge (top) and L_3 edge (bottom) and the respective differential absorption images. **D, E** Same for Cu pre- and L_3-edge. **F, G** The respective two-dimensional projections over *Z*-axis and 3D segmentation model (**H,I**). (**J-L**) Subspherical object resembling a cell acquired at 520 eV, Fe and Cu L_3 pre-edge/edge energies. **M, N** Integrated Fe and Cu L_3-edge XANES spectra for Cu–Fe mineral phase and selected reference mineral samples. (*) Note that the reference spectrum for chalcopyrite was reproduced from Goh et al. (2006)[27]. MComp microcompartments, Gt goethite.

would have provided abundant precursors for the subsequent formation of chalcopyrite[13,15,16,26]. Collectively, these data justify the widespread availability of Cu sulfide precursors, which transformed into chalcopyrite towards the end of the incubation.

Geochemical considerations and chalcopyrite formation model

The conclusions drawn from plots 7A–C indicate that, with all the reactants present in excess in the solution, covellite and chalcopyrite precipitation will occur if sufficient time is given for the reaction, and the existing kinetic barriers can be overcome. However, when S^{2-} (as H_2S) is considered to be the limiting factor controlling sulfide mineral formation—a common scenario in most AMD systems—the studied system may be observed from a micro-, nano-, or pico-molar scale. This is more reflective of the conditions existing in the microenvironments surrounding microbial cells (e.g. sulfate-reducing bacteria) in the natural environment. At the micro-scale, H_2S is present at low concentrations in isolated and strongly reducing microenvironments, for instance around sulfidogenic microbial cells. Previous 16S rRNA gene amplicon investigations of the microbial community composition in the IC after 18 months of incubation showed the high relative abundance of reads classified as *Desulfosporosinus*, *Acididesulfobacillus* and *Desulfurispora* (Supplementary Fig. 2)[16], genera known to contain SRB. Their sulfidogenic activity was further supported by the observed increase in pH in the bulk liquid over time, a consequence of microbial sulfate reduction at acidic pH (Supplementary Fig. 2)[26,29]. Around these sulfidogenic microbial cells, in a µm- to nm-scale chemical gradient may be envisaged with H_2S or HS^- species (depending on pH conditions) being concentrated only in their immediate vicinity, while sulfide concentrations would be extremely low to non-existent in the bulk solution. In addition, the existing sulfide released by the SRB may also react with a number of different metal cations, such as Fe(II), Zn(II), Cd(II), Pb(II) or Cu(II), which would compete for the sulfide ligand and thus lead to sulfide depletion in the bulk solution.

The calculations shown in Fig. 7D suggest that the formation of the Cu and Cu–Fe sulfides would only occur in conditions of pe<2 (Eh <100 mV). Such reducing conditions have never been detected in the bulk liquid fraction extracted from the respective sediment layer and measured with conventional electrodes (Fig. 8), making it logical to assume that these chemical conditions would have only existed in the immediate surroundings of the bacterial cells, when H_2S/S^{2-} availability would be localized (Fig. 7E). Previous studies have shown that under these reducing conditions, the Cu cations in solution are primarily Cu(I), rather than Cu(II)[30], indicating that Cu speciation in these microenvironments plays an important role in the mineralogy of the resulting copper sulfides. The pH does not appear to considerably influence the formation of these minerals, so the concept of "microniches", often proposed to account for chalcopyrite formation[10,12] would pertain primarily to sulfide availability for metal binding and sulfide formation. However, this microniche hypothesis applies specifically to SRB. In other cases, such as the one illustrated in Fig. 6, where chalcopyrite

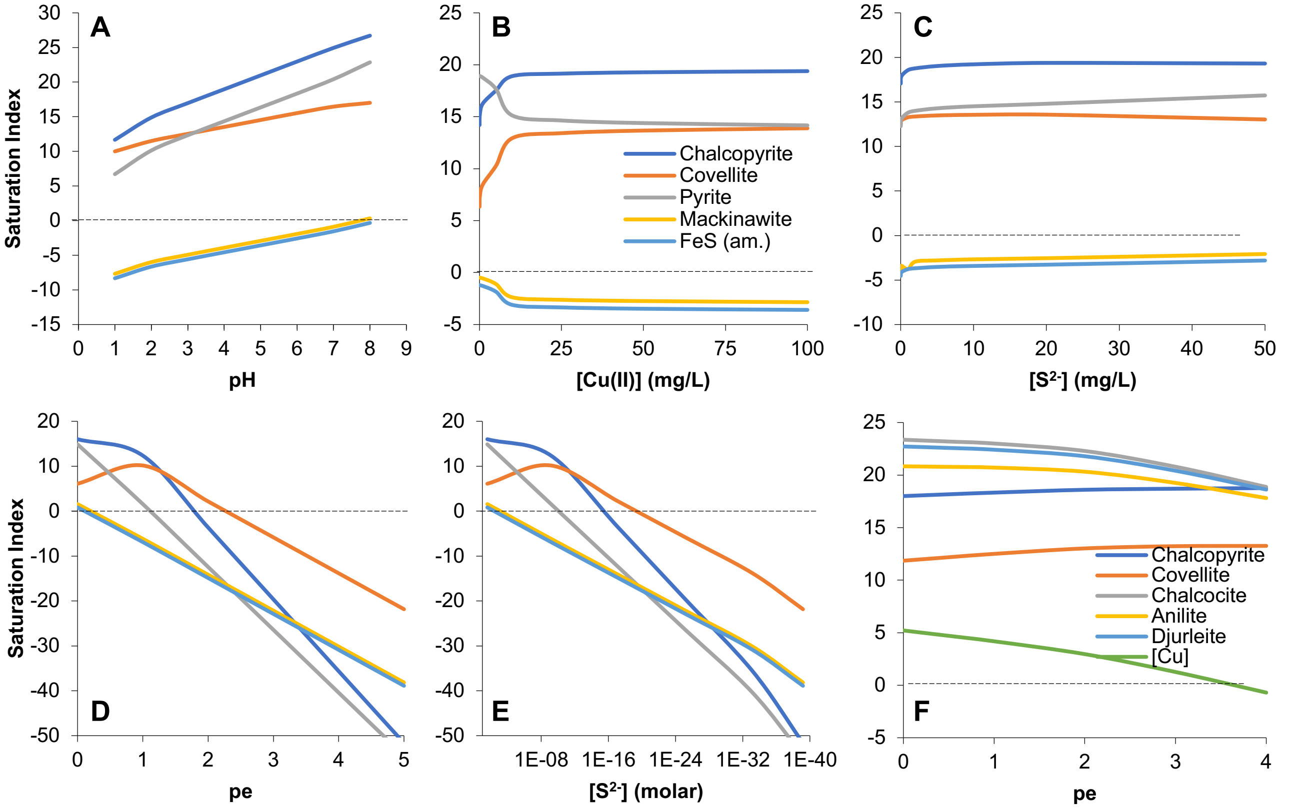

Fig. 7 | Binary plots showing the dependence of the saturation index (SI) of selected sulfide minerals and metallic copper on different chemical variables such as pH, pe, and concentrations of Cu(II) and S^{2-}. For (**A**–**F**), calculations were conducted in PHREEQC using the chemical conditions provided in Supplementary Table 3. Sulfides include chalcopyrite, covellite, chalcocite, anilite, djurleite, pyrite, mackinawite and amorphous FeS. Electronic potential is defined as pe = Eh/59.2. The dashed horizontal line depicts in all cases the value of SI = 0 separating the saturation (precipitation) and undersaturation (dissolution) fields.

crystals grow around other type of cells (e.g. eukaryotic), the hypothesis described above would not be applicable.

An alternative and intriguing proposed mechanism for chalcopyrite formation in AMD environments considers that its precipitation is not solely governed by the concentration of H_2S along a micro- or nano-gradient between a bacterial cell membrane and the bulk solution, but also by the valence state of the Cu cations in solution. This valence state could determine if an intermediate copper sulfide mineral precursor forms, eventually leading to chalcopyrite after a recrystallization through the exchange of Cu and Fe atoms between the pre-existing Cu–S crystal and the bulk solution. According to this hypothesis, the role of SRB cells is primarily to provide sulfide ions necessary for sulfide mineral formation, but they may not be essential for the nucleation and precipitation of chalcopyrite in Cu-rich acidic waters. This process could also occur around other types of cells and/or organic structures (e.g., living or dead cells and their exudates) which can provide sufficiently reducing conditions for the formation of copper sulfide mineral precursors. The precipitation of Cu sulfide linked to collapsed organic frameworks has been previously described in the cryogenized sample from Cueva de la Mora pit lake[26]. The need for a mineral precursor was initially discussed by Cowper et al.[10]. Nevertheless, our observations and theoretical calculations strongly suggest that, in our study, the process of chalcopyrite formation most closely resembles the mechanism proposed by Mansor et al.[12]. This model proposes the initial formation of an intermediate Cu–S mineral precursor, followed by Fe enrichment at the outer rims of the crystals as iron cations are incorporated from the bulk solution, ultimately resulting in recrystallization into chalcopyrite. This hypothesis is strongly supported by the images presented in Fig. 2C, D.

It must be noted that the oxidation state of the iron cations in the chalcopyrite structure are necessarily Fe(III)[27], which could not be sourced directly from the Fe-rich bulk environment at the Eh below 400 mV[31]. Instead, the plausible source of the ferric iron in the acidic sediments could be related to the release of Fe^{3+} during the transformation of the early Fe (oxy)hydroxides (schwertmannite and jarosite) to goethite, before it would have got reduced to Fe(II) by the reductive Eh of the medium[26]. Alternatively, we hypothesize that the ferrous iron from the bulk medium could have been oxidized by Cu(II) ions as was previously suggested in other environments[32]. In addition to the divalent copper being the most probable speciation at the redox conditions measured in the sediments, it could potentially come from the parent copper sulfides. Even though the oxidation state of Cu in sulfides remains a matter of debate, some authors suggest that covellite contain a mixture of valences such as $(Cu^{+})_2(Cu^{2+})(S^{2-})(S_2)^{2-}$[17], $[(Cu^{+})_2(S_2^{2-})(Cu^{+})(S^{2-})]-1$electron or $[(Cu^{(1+\delta)+})_2(S_2^{2(1-\delta)-})(Cu^{(1+\delta)+})(S^{(2-\delta)-})]$ with $\delta = {}^1/_6$[33]. Given that chalcopyrite is purely a Cu(I) phase[18], the hypothesized oxidation of Fe(II) by Cu(II) might be an important mechanism for elimination of the divalent copper from the final transformation product. The model proposed to explain the formation of chalcopyrite in low-T aqueous systems is schematically illustrated in Fig. 9.

Overall, this paper highlights the importance of microorganisms in chalcopyrite formation at low temperature and under acidic and metal-rich conditions, not only as active suppliers of the reactants needed for mineral formation (S^{2-}, Fe(II), Cu(I)) but also as passive templates providing microenvironments with the required chemical conditions for crystal nucleation and growth. Besides, our work shows that the study of complex metal–microbe–mineral interactions leading to mineral formation in chemically extreme aqueous systems and subsurface environments can only be achieved through a combination of different high-resolution techniques (e.g., STEM, HRTEM, XAS, cryo-TXM), which allows the observation of these interactions in heterogeneous natural soil matrix from different perspectives.

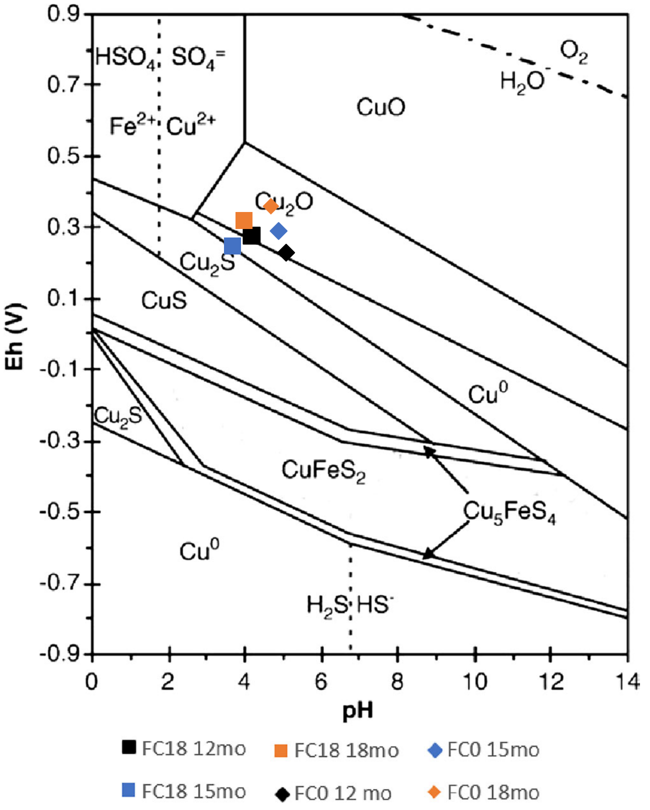

Fig. 8 | Experimental Eh and pH values projected onto a Pourbaix diagram of Cu–Fe–S–O–H system at 25 °C. Fe oxides and Fe sulfides were suppressed for simplification. The total dissolved activities were assumed such as Cu: 10^{-6}, Fe: 10^{-6} and S: 10^{-3}. Legend: mo months of incubation. Modified after diagram from ref. 25.

Methods

Studied sites and sampling

For this study Filón Centro (FC) (37°35'27.4"N, 7°07'27.5"W) APL was considered. Being a part of the Tharsis mines, is among the westernmost mines in the Iberian Pyrite Belt (IPB), located in the South of the Iberian Peninsula (Huelva, Spain). Filón Centro is characterized by a Variscan-aged hydrothermal system within the IPB, spanning the Late Devonian to Early Carboniferous period, encompassing a vast stratabound, volcanogenic massive sulfide (VMS) district[34]. The regional geology is dominated by a volcanic-sedimentary sequence comprising felsic to intermediate metavolcanic rocks, interbedded with shales, siltstones, and minor cherts. The mineralization at FC is associated with the juxtaposition of stockwork and massive sulfide orebodies, predominantly composed of pyrite (>90% of volume) with minor amounts of chalcopyrite and sphalerite, within the aforementioned metavolcanic host rocks[35]. This altogether defined the chemical composition of the APL water balancing between the acidity and alkalinity inputs into the lake, as well as the neutralization processes in the water column. Structural complexity within the deposit is evident through the presence of thrust faults, folds, and steeply dipping veins, controlled by the regional Variscan orogeny.

The area was extensively mined by the Tartessians, Phoenicians, Carthaginians, Romans and Moors[26,36]. In the XIX century, Tharsis Mines witnessed an important development, promoted by British companies, who invested in the area, introducing modern technologies to improve extraction efficiency for Cu, Pb, and Zn. The Tharsis Sulfur and Copper Company, founded in 1866, played a key role in expanding the mining infrastructure, including railways and port facilities. Despite the fluctuating metal prices and labor disputes, mining continued well into the XX century, with the interruption between 1882 and 1956. However, the decline of the industry in the second half of the XX century, falling metal prices, high operating costs and environmental concerns led to the final closure of Filón Centro in 2000[34]. Currently, the lake shows an extension of 3.6 ha (430 m by 140 m) with a maximum depth of 50 m.

Mixolimnetic sediment was directly gathered with a shovel from the shallow shore (<0.5 m depth). Monimolimnetic anoxic sediment was collected using a USC 6000 gravity corer (Uwitec, Mondsee, Austria) and exchangeable polycarbonate tubes of 60 cm length and 9 cm in diameter. For the sediment from 18 m depth in Filón Centro (FC 18), both water and sediment, recovered in the tube, were hermetically capped until the arrival to the University of the Basque Country (UPV/EHU). The sediment from the deepest point of the lake (50 m) was sampled in two campaigns using a 5 L Van Dorn sampling bottle (KC, Silkeborg, Denmark) and the gravity corer setup described above, recovering the lake bottom mixed sediment of top centimeters. The preparation and evolution of the incubation column experiment has been previously described in refs. 16, 26.

Sediment and pore-water geochemistry

For the quantification of the microbially-mediated metal immobilization, at the end of 18mo incubation of the ICs, the sediments of the columns were extruded (using an Uwitec core cutter), transferred to 15 mL Falcon tubes and sealed with silicone. For each set of columns, two or three equivalent samples (same depth, same initial material) were obtained from more evolved and least evolved ICs (e.g., FC18 −1 cm from glycerol-amended vs −1 cm untreated IC). By the comparison of these results, the contribution of microbial activity to the metal immobilization could be established. These samples were obtained from the most reactive horizons of the ICs, i.e., normally from the top 1–2 cm of the sediment column. Samples were stored at 4 °C and subsequently sent to the University of Alberta (Edmonton, Canada) for geochemical analysis.

Upon arrival, 15 mL (solid + liquid) of initial sediment samples were centrifuged at 17,500*g* in Sorvall LYNX 4000 superspeed centrifuge (ThermoFisher Scientific, Waltham, MA, US) for 15 min. Supernatant was filtered through 0.22 μm nylon membranes to remove residual suspended particulate matter and acidified with 10 μL of 70% nitric acid (HNO_3, Thermo Fisher Scientific) for further chemical analyses by ICP-MS. For the ICP-MS analyses, an aliquot of 0.5 mL of the filtered and acidulated liquid phase was diluted 20-fold with the mixture of 2% nitric acid and 0.5% hydrochloric acid.

The solid fraction was transferred into a plastic tray and dried for at least 3 days at 35 °C in the laboratory oven. Subsequently, samples were grinded in an agate mortar and 100 mg were separated in a 50 mL Falcon tube. Each sample was triplicated and for each batch of 4 samples (12 falcons), 2 empty tubes were added and used as blank. These empty tubes received exactly the same treatment as the ones containing solid samples.

The sequential extraction protocol, used in this study, was a combination of those proposed by[37–39], and it appears summarized in the Table 2 below. For each sample and at each step, 10 mL of extracting solution was added. After completing each step, samples were centrifuged at 17, 500*g* and 3 mL of solution was extracted. The remaining liquid was discarded and the solid phase washed with MilliQ water and stored for the next step in the same falcon tube. To achieve the appropriate TDS range for the ICP-MS analyses, the 3 mL aliquots were diluted with 47 mL of a mixture of 2% nitric acid and 0.5% hydrochloric acid. For steps 1–4, before analyzing, samples were additionally diluted 1–4-fold with the same mixture of acid as mentioned before, while aliquots from steps 5 and 6 were analyzed with no further dilution.

Diluted samples were analyzed on an 8800 Triple Quadrupole ICP-MS (Agilent, Santa Clara, CA, US) at the Environmental Geochemistry Lab (University of Alberta). The instrument was run in high matrix mode using argon (Ar) gas as the carrier and dilution gas. An internal standard solution, including all relevant elements, was prepared with a certified standard solution with a known concentration. For the calibration line, this internal standard was diluted 5, 25, 125, and 625 times, by pipetting 2 mL of the previous solution and diluting it with 8 mL of a mixture of 2% nitric acid and 0.5% hydrochloric acid.

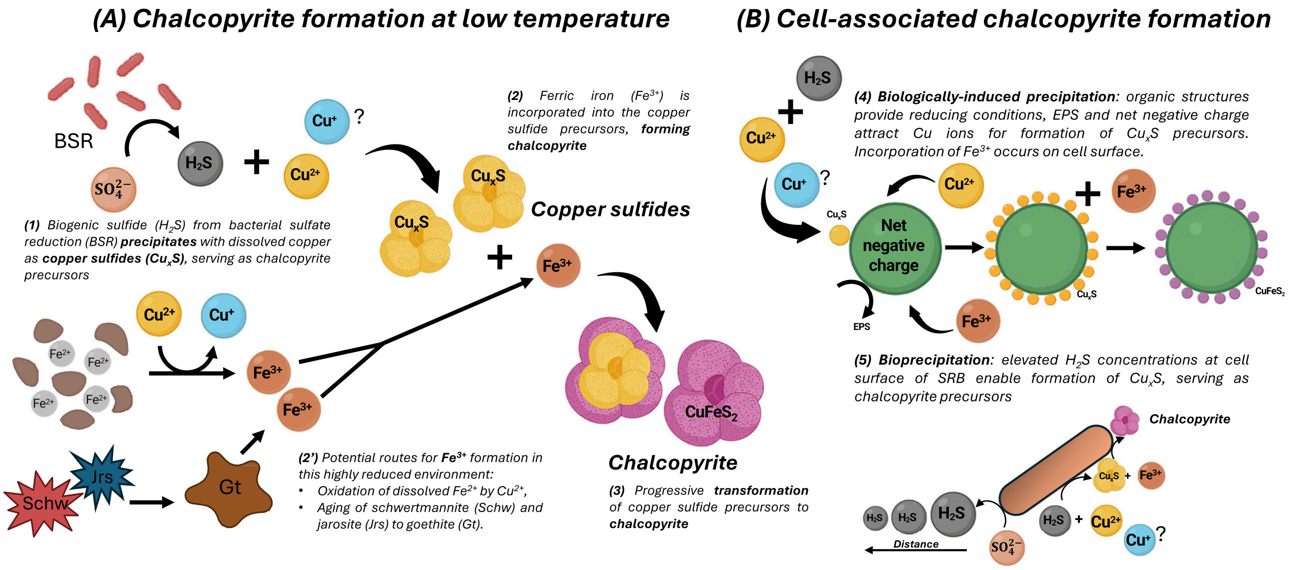
(A) Chalcopyrite formation at low temperature

(B) Cell-associated chalcopyrite formation

(1) Biogenic sulfide (H_2S) from bacterial sulfate reduction (BSR) **precipitates** with dissolved copper as **copper sulfides (Cu_xS)**, serving as chalcopyrite precursors

(2) Ferric iron (Fe^{3+}) is incorporated into the copper sulfide precursors, **forming chalcopyrite**

(2') Potential routes for Fe^{3+} formation in this highly reduced environment:

- Oxidation of dissolved Fe^{2+} by Cu^{2+},
- Aging of schwertmannite (Schw) and jarosite (Jrs) to goethite (Gt).

(3) Progressive **transformation** of copper sulfide precursors to **chalcopyrite**

(4) Biologically-induced precipitation: organic structures provide reducing conditions, EPS and net negative charge attract Cu ions for formation of Cu_xS precursors. Incorporation of Fe^{3+} occurs on cell surface.

(5) Bioprecipitation: elevated H_2S concentrations at cell surface of SRB enable formation of Cu_xS, serving as chalcopyrite precursors

Fig. 9 | Schematic representation of the possible mechanisms of microbially induced chalcopyrite precipitation identified in this study. Stages: (**1**) Bacterial sulfide production and precipitation of the early Cu sulfides; (**2**) Incorporation of Fe by the Cu sulfide precursor; (**2'**) Possible origin of ferric iron in the reduced environment, including oxidation of ferrous iron by cupric ion in pore water in the sediment and/or release of ferric iron during aging of the schwertmannite- and jarosite-rich sediment to goethite-rich sediment (**3**) Gradual transformation to chalcopyrite from the grain borders to the core of the Cu sulfide; (**4**) Biologically induced precipitation pathway, with limited involvement of the cells (particularly eukaryotic), which create locally higher concentration of ions (electrostatic attraction and EPS) and more reductive conditions which triggers Cu sulfide precipitation and further transformation to chalcopyrite as mentioned above; (**5**) Bioprecipitation pathway involving an active role of sulfate-reducing bacteria in generating locally higher concentrations of H_2S, which would promote the precipitation of the Cu sulfide and further transformation to chalcopyrite. Schw schwertmannite, Jrs jarosite, Gt goethite, Cu_xS copper sulfide precursor.

Table 2 | Sequential extraction (SqExt) procedure was used in this study for selective dissolution

Step	Reagent	Experimental conditions	Expected dissolving phases
Step 1	1 M $MgCl_2$	Shaken for 2 h	Water soluble and exchangeable ions
Step 2	1 M CH_3COONa adjusted to pH 4.5 with CH_3COOH	In laboratory furnace at 50 °C and 48 h	Carbonates, including siderite and ankerite
Step 3	1 M Hydroxylamine–HCl in 25% v/v CH_3COOH	Shaken for 48 h	Poorly crystalline oxides-hydroxi(sulfates) (e.g., ferrihydrite or schwertmannite)
Step 4	0.2 M Na-citrate buffered to pH 4.8 with CH_3COOH	Shaken for 2 h	Reducible crystalline oxides (e.g., jarosite and goethite)
Step 5	0.2 M NH_4-oxalate buffered to pH 3.2 with 0.17 M oxalic acid	Shaken for 6 h	Non-reducible crystalline oxides (e.g., magnetite)
Step 6	30% H_2O_2	In laboratory furnace at 80 °C for 2 h	Organic carbon and secondary sulfides

Based on refs. 37–39. Aliquots were obtained before and after each step for Differential X-ray Diffraction (DXRD)[26].

Geochemical modeling. The software package PHREEQC version 3.0.5-7748[40] was used to estimate the saturation indices (SI) for common metal sulfide minerals. Physico-chemical parameters (e.g., pH, ORP, T) measured during incubation and all ionic species present in the pore waters were used as the input parameters. The ionic strength of the samples ranged between 0.60 and 0.76, being comparable to seawater values, which is typically considered as the threshold for applying the Davies equation of ionic activity coefficients in dilute solutions[41,42]. The Wateq4f.dat thermodynamic database[43] was selected for all calculations.

Electron microscopy (SEM + STEM)

Sediment samples were characterized by scanning electron microscopy (SEM) at the Electronic Microscopy and Material Microanalysis Service of SGIker facilities of the University of the Basque Country (UPV/EHU). These samples were washed with MilliQ water in several cycles of repeated centrifugation at 13,200 rpm (Eppendorf 5415D), liquid phase elimination, water addition and re-suspension. Just before pipetting a sample drop, samples were sonicated in an ultrasonic bath (J.P. Selecta 3000513, Abrera, Spain). Afterwards these were mounted on 25 mm graphite stub, subjected to plasma cleaning and coated with C layer and analyzed under JEOL JSM-7000F field emission SEM (10 mm working distance, 20 kV, 1 nA) coupled with Oxford INCA 350 energy dispersive X-ray spectroscopy (EDX) for semi-quantitative point chemical analysis. The EDX was calibrated with the reference Cu foil. Raw X-ray intensity values were ZAF corrected using the INCA 350 software (Oxford Instruments, Abingdon, UK) with a set of standards for quantification.

Additionally, STEM was also used to further investigate the elemental composition and identify the mineral phase. For this, the solid fraction was resuspended in MilliQ water in an Eppendorf tube and sonicated. Afterwards, a small volume of 3–5 µL was pipetted onto holey carbon-coated TEM support Ni grids (300 Mesh). Imaging (high-angle annular dark field (HAADF), Bright Field (BF), High-resolution transmission electron microscopy (HRTEM) modes), compositional point analysis or mapping (EDX) and selected area electron diffraction (SAED) analyses of neoformed sulfides were performed on FEI Talos F200i STEM (ThermoFisher Scientific, Oregon, USA) operated at 200 KeV and incorporating Bruker X-Flash EDX system at Polymer Characterization Service of the SGIker facility (UPV/EHU).

X-ray absorption spectroscopy

X-ray Absorption Spectroscopy (including XANES and EXAFS) were collected at the BM20 Rossendorf Beamline (ROBL) at the European Synchrotron Radiation Facility (ESRF) in Grenoble (France)[44]. X-ray Absorption Spectroscopy was used to investigate the sediment samples from the incubation column experiment due to several advantages over other techniques. Firstly, the inspection of the XANES, dictated by the absorption of the incident X-rays by an atom, allowed the investigation of the electronic structure of the unoccupied levels, providing information on the electronic configuration, vacant orbitals, oxidation states and coordination geometry of the absorbing atom[45]. Secondly, it must be taken into consideration the Extended X-Ray Absorption Fine Structure (EXAFS), described as the interference of the outgoing wave and the scattering of the photoelectron wave from the emitter at the neighboring atoms, shows good sensitivity to low-crystalline solids and the unique capacity of the analysis of local atomic environment for each type of atom[46]. Unlike XRD, for some elements (e.g., Cu and Zn, but not for Fe) XAS allows to avoid the contribution of detrital and oxidized precipitates (e.g., goethite or clays), predominant in the sediment sample, and separately investigate the structure of low crystalline neoformed metal sulfides. Additionally, being a whole-sample representative analysis, it allowed contrasting the qualitative data from the electron microscopy on the neoformed mineral phases, complementing the list with those not observed by other techniques (e.g., too small, dispersed, etc.). Finally, EXAFS allows the estimation of the relative abundances of different components in the sample by PCA, which is not possible using other techniques.

Sample preparation

Sediment samples from the ICs were extracted with 25 mL syringes after 15 mo of incubation. Syringes were immediately sealed with silicone and uncapped only inside the glovebox under controlled N_2 atmosphere. This was carried out inside the glove box (Plas-Labs, Lansing, MI, US) at the Materials Physics Center (CFM-CSIC, Donostia, Spain). Samples were transferred to 40 mL Nalgene Oak Ridge tubes, tightly capped inside the glovebox and settled down at 17,500 g in Sigma 3−16 P (Fisher Bioblock Scientific, Madrid, Spain) centrifuge. After discarding the supernatant water, the settled sediment slurry was transferred with two spatulas to fill the cavity of the sample holder for XAS experiment, sealed with Kapton tape on both sides and transferred to a 3.15 L cryogenic dewar (US Solid, Hayward, CA, US) filled with liquid nitrogen (N_2(l)). The storage and shipping were performed at constant N_2(l) conditions to guarantee stable anoxic conditions and inhibit mineral transformations.

Reference materials were prepared at the ESRF BM20 laboratory using natural monomineralic samples, similar to the minerals expected to be detected in the sediment. The purity of each sample was confirmed by XRD and SEM if needed. Pellets were prepared by pressing the mixture of finely ground reference mineral with 100 mg of boron nitride (BN), as a filler transparent to X-rays in the energy range of interest. The amount of the reference in the mixture was equivalent to the edge jump of 1.0, calculated based on the individual cross-section of each element[47] and individual weight proportion of the element in each mineral structure (webmineral.com).

XAS measurements. The measurements were carried out at 15 K in a closed-cycle He cryostat (CryoVac GmbH, Germany), which allowed for the inhibition of any possible photon-induced redox modifications, along with improving the signal quality by eliminating thermal or vibrational contributions to the Debye-Waller factor. The spectra were recorded in fluorescence mode at the Cu K-edge (8978.9 eV) using an 18-element Ge-detector (Mirion Technologies, Canberra) coupled with complementary-metal–oxide–semiconductor (CMOS)-based charge-sensitive Cube amplifiers (XGLab, Milano, Italy). Simultaneously, Cu metal foil was systematically measured in transmission mode and further used for energy calibration between different spectra. The incident energy was selected by Si (111) double-crystal monochromator and higher harmonics were suppressed by two Rh-coated mirrors.

Data evaluation. The experimental results were compared to the theoretical calculations. The experimental data reduction was performed in Sixpack[48] and WinXAS[49] software. Firstly, from the experimental absorption spectra, the background absorption was removed by subtraction of a Victoreen-type polynomial (1st degree for pre-edge and 2nd degree for post-edge). The oxidation state was determined by comparing the sample XANES to the reference patterns. The threshold energy (E_0) was defined as the first inflexion point of the absorption edge. Subsequently, the EXAFS oscillations were extracted by a cubic-spline fit, with the number of splines suggested by the program (typically 6), in the range from 2.0 to ~10.0 $Å^{-1}$. Afterwards, the k^3-weighted EXAFS function (accounting to attenuation effects) was Fourier-transformed using a Bessel window with parameter 3 across the available k-space.

For the comparison, the theoretical phase shifts and effective backscattering amplitudes for shell fit were calculated with the FEFF 8.2 code[50]. Previously, atomic clusters around the excited atom with a radius of sphere of 8 Å were generated in Demeter pack[51]. The shift in threshold energy (ΔE_0) was varied as a global parameter in the fit procedure for all shells and the amplitude factor was set to a value of 0.9. Other parameters, such as coordination numbers, interatomic distances, Debye–Waller factor, and Fermi energy value were determined by iterating the least square fit between the experimental and theoretical absorption spectra.

Transmission X-ray microscopy

Cryogenic samples were investigated by synchrotron-based cryo-transmission soft X-ray microscopy (TXM) at the MISTRAL beamline (BL-09) of ALBA synchrotron facility (Cerdanyola del Vallès, Spain)[52]. This energy-dependent transmission microscopy exploits a contrast mechanism based on the intensity loss of the transmitted X-ray beam. Varying the energy range across element-specific absorption edges generates contrast based on the chemical and electronic structure of the sample. In the water window energy range (280–530 eV) the contrast between carbon-rich membranes and water rich cytoplasm is optimized. This technique allows the image acquisition of unstained and intact biological samples in its almost native state[53].

Sample preparation. For this experiment, a new incubation column FC18 was set with the water and sediment from the lake and amended with glycerol (following the same procedure described previously). After 6 months of incubation, ICs were extruded and dark sediment layers were recovered in triplicated aseptic 1.5 mL Eppendorf tubes, sealed with silicone and stored at 4 °C.

Cryogenic sample preparation and screening were performed at the Biological Laboratory of the ALBA synchrotron. For the sample dilution, MilliQ water was previously deoxygenized by purging it with N_2 gas for 20 min. The sediment samples were diluted with deoxygenized water, mixed and 2 μL of the supernatant were transferred onto Au Quantifoil G200F1 R 2/2 grids (Micro Tools GmbH, Jena, Germany) pretreated with 1.5 μL of Au 100 nm bits' (EMGC100, BBI Group, Cardiff, UK) suspension. Afterwards, samples were vitrified following plunge freezing protocol in liquid-N_2-cooled liquid ethane using Leica EM GP2 Vitrobot (Leica Microsystems, Wetzlar, Germany) with the working condition in the blotting chamber of 20 °C, humidity 90% and blotting time between 3–6 s. After plunge freezing, each grid was screened under Zeiss AxioScope A1 (Carl Zeiss Microscopy GmbH, Jena, Germany) light microscope. During this process, the cryogenic conditions were preserved using Linkam CMS196 cryo-correlative microscopy stage (Linkam Scientific Instruments Ltd, Redhill, UK). Finally, after quality control, selected grids were stored onsite at liquid N_2 until the allocated beamtime.

TXM measurements. Initially, to define the best regions in each grid, in terms of transparency, quality of ice or abundance of microbial cells, an image of the full grid was obtained with a visible light microscope installed in the TXM chamber and coordinated with the X-ray beam. Then, from the polychromatic radiation coming from the bending magnet, specific energies were selected using a variable line spacing plane grating monochromator. This incident beam was tuned at a 520 eV for a first inspection of selected regions on the grid, by the mean of "mosaics" images, i.e., composition of many fields of view of about 100 µm by 100 µm. Afterwards, on selected field of views, the energy was moved across the Fe and the Cu L_3 edges for the acquisition of the spectromicroscopy data. Magnified images of the sample (1–2 s exposure time, 11.8 nm effective pixel size and field of view of about 13 by 13 µm), produced by a Fresnel Zone Plate objective lens, were acquired on a PIXIS-XO (Teledyne Princeton Instruments, Trenton, NJ, US) CCD detector. At the Cu L_3 edge, a binning 2 was used to minimize the radiation damage. During spectromicroscopy acquisition, the Zone Plate and CCD were moved automatically with the energy to keep the sample in focus and the magnification constant, respectively. Spectral sampling was varied between 0.10-0.25 eV and the total acquisition time of an energy scan of 10 areas of interest was about 2 h for each edge, including the flat field acquisition at each energy step. The exact position of the Fe and the Cu L_3 edges was established at the beginning of the experiment, using a mix of different reference minerals (chalcopyrite, goethite and covellite). These reference materials were prepared by finely hand-grinding pure mineral phases in an agate mortar. For the proper mingling, several minerals were mixed in the mortar and further ground together in the presence of absolute ethanol, 2µL of that suspension was pipetted onto Au Quantifoil G200F1 R 2/2 grids and suspended in liquid N2 for cooling down to the experimental conditions.

Finally, on the field of views which showed the presence of Fe and Cu from spectromicroscopy, to clarify the three-dimensional distribution of the detected phases and relation to the microbial structures, tomography at 520 eV was performed. The tilted series were recorded on a tilt range of -65° to +65° and 1° increment and an acquisition time of 1–2 s per image. Samples remained at a controlled temperature of 100 K during all the experiments.

Data evaluation. These tomography tilt series were processed with a suite of programs to generate volume reconstructions. Firstly, tilt series were aligned using eTomo tomography processing software from the Imod package[54]. It was used for fine stacks' alignment by gold nanobits tracking and tilt axis adjustment. Subsequently, the aligned tilt series were reconstructed in TOMO3D software[55], using GPU-based Simultaneous Iterative Reconstruction Technique (SIRT) with 30 iterations. The results were saved as stacks of X-Y plane images (orthogonal plane with respect to X-rays direction), which were sliced along the Z-axis (optical axis) with a fixed step size. Finally, these were segmented in the Amira software pack (Thermo Fisher Scientific, Waltham, MA, USA) to create volume rendering of 3D features of the cells and mineral precipitates. Being the minerals well visible also at 520 eV, this approach allows extending from 2D to 3D the localization of metal-rich regions and, for instance, clarifying the eventual presence of certain precipitates on the external or internal microbial membrane.

To obtain L-edge XANES, each image of the energy stack (I) was normalized to unity by dividing by the corresponding flat field image (I0), recorded under the same conditions after each micrograph. After stack alignment, the transmittance was then converted to absorbance (A) using the Beer-Lambert law. The selection of the pixels containing Fe or Cu and the extraction of the absorbance signal was performed using TXMWizard software[56], obtaining Fe and Cu L_3-edge X-ray absorption spectra. Pixels containing Fe or Cu were defined as those with a signal-to-noise ratio >2, where the signal was defined as the difference between the average absorbance value around metal L3-edge maxima (±0.3eV) and the average value in the pre-edge and noise as the signal standard deviation in the pre-edge energy region.

Reporting summary

Further information on research design is available in the Nature Portfolio Reporting Summary linked to this article.

Data availability

All data underlying the graphs and charts presented in this study have been deposited in the Figshare repository. The dataset is publicly available at dx.doi.org/10.6084/m9.figshare.30104023.

Received: 25 February 2025; Accepted: 3 October 2025;

References

1. Deer, W. A., Howie, R. A. & Zussman, J. *An Introduction to the Rock-Forming Minerals* (Mineralogical Society of Great Britain and Ireland, 2013). https://doi.org/10.1180/DHZ.
2. Velasco, F., Herrero, J. M., Gil, P. P., Alvarez, L. & Yusta, I. Mississippi Valley-Type, Sedex, and Iron Deposits in Lower Cretaceous Rocks of the Basque-Cantabrian Basin, Northern Spain. in *Sediment-Hosted Zn-Pb Ores* (eds. Fontboté, L. & Boni, M.) 246–270 (Springer Berlin Heidelberg, 1994). https://doi.org/10.1007/978-3-662-03054-7_15.
3. Hedenquist, J., Arribas, A. & Gonzalez-Urien, E. in *Gold in 2000* (eds. Hagemann, S. & Brown, P.) 13 (Society of Economic Geologists, 2000).
4. Eremin, N. I., Dergachev, A. L., Sergeeva, N. E. & Pozdnyakova, N. V. Types of volcanic-hosted massive sulfide deposits. *Geol. Ore Depos.* **42**, 160–171 (2000).
5. Candela, P. A. Ores in the Earths Crust. *Treatise Geochem.* **3**, 659 (2003).
6. Rusk, B. G., Reed, M. H. & Dilles, J. H. Fluid inclusion evidence for magmatic-hydrothermal fluid evolution in the porphyry copper-molybdenum deposit at Butte, Montana. *Economic Geol.* **103**, 307–334 (2008).
7. Mungall, J. E. Crystallization of magmatic sulfides: an empirical model and application to Sudbury ores. *Geochim. Cosmochim. Acta.* **71**, 2809–2819 (2007).
8. Zhao, J., Brugger, J., Chen, G., Ngothai, Y. & Pring, A. Experimental study of the formation of chalcopyrite and bornite via the sulfidation of hematite: Mineral replacements with a large volume increase. *Am. Mineralogist* **99**, 343–354 (2014).
9. Gartman, A., Findlay, A. J. & Luther, G. W. Nanoparticulate pyrite and other nanoparticles are a widespread component of hydrothermal vent black smoker emissions. *Chem. Geol.* **366**, 32–41 (2014).
10. Cowper, M. & Rickard, D. Mechanism of chalcopyrite formation from iron monosulphides in aqueous solutions (<100°C, pH 2–4.5). *Chem. Geol.* **78**, 325–341 (1989).
11. Hochella, M. F. et al. Direct observation of heavy metal-mineral association from the Clark Fork River Superfund Complex: Implications for metal transport and bioavailability. *Geochim. Cosmochim. Acta.* **69**, 1651–1663 (2005).
12. Mansor, M., Berti, D., Hochella, M. F. Jr, Murayama, M. & Xu, J. Phase, morphology, elemental composition, and formation mechanisms of biogenic and abiogenic Fe-Cu-sulfide nanoparticles: s comparative study on their occurrences under anoxic conditions. *Am. Mineralogist* **104**, 703–717 (2019).
13. Diez-Ercilla, M., Sánchez-España, J., Yusta, I., Wendt-Potthoff, K. & Koschorreck, M. Formation of biogenic sulphides in the water column of an acidic pit lake: biogeochemical controls and effects on trace metal dynamics. *Biogeochemistry* **121**, 519–536 (2014).
14. Sánchez-España, J., Yusta, I., Ilin, A., van der Graaf, C. & Sánchez-Andrea, I. Microbial geochemistry of the Acidic Saline Pit Lake of Brunita Mine (La Unión, SE Spain). *Mine Water Environ.* **39**, 535–555 (2020).
15. van der Graaf, C. M. et al. Biosulfidogenesis mediates natural attenuation in acidic Mine Pit Lakes. *Microorganisms* **8**, 1275 (2020).
16. Ilin, A. M. et al. Glycerol amendment enhances biosulfidogenesis in acid mine drainage-affected areas: an incubation column experiment. *Front. Bioeng. Biotechnol.* **10**, 978728 (2022).
17. Evans, H. & Konnert, J. Crystal structure refinement of covellite. *Am. Mineral.* **61**, 996–1000 (1976).

18. Pearce, C. I., Pattrick, R. A. D., Vaughan, D. J., Henderson, C. M. B. & Van Der Laan, G. Copper oxidation state in chalcopyrite: Mixed Cu d9 and d10 characteristics. *Geochim. Cosmochim. Acta.* **70**, 4635–4642 (2006).
19. Wyckoff, R. W. G. *Crystal Structures* (Interscience Publishers, 1964).
20. Rossberg, A., Reich, T. & Bernhard, G. Complexation of uranium(VI) with protocatechuic acid? Application of iterative transformation factor analysis to EXAFS spectroscopy. *Anal. Bioanal. Chem.* **376**, 631–638 (2003).
21. Scheinost, A. C. et al. Quantitative antimony speciation in shooting-range soils by EXAFS spectroscopy. *Geochim. Cosmochim. Acta.* **70**, 3299–3312 (2006).
22. Yalçıntaş, E., Scheinost, A. C., Gaona, X. & Altmaier, M. Systematic XAS study on the reduction and uptake of Tc by magnetite and mackinawite. *Dalton Trans.* **45**, 17874–17885 (2016).
23. Takéuchi, Y., Kudoh, Y. & Sato, G. The crystal structure of covellite CuS under high pressure up to 33 *kbar*. *Z. Kristallographie* **173**, 119–128 (1985).
24. Mardanov, A. V. et al. Genomic insights into a new acidophilic, copper-resistant Desulfosporosinus isolate from the oxidized tailings area of an abandoned gold mine. *FEMS Microbiol. Ecol.* **92**, fiw111 (2016).
25. Córdoba, E. M., Muñoz, J. A., Blázquez, M. L., González, F. & Ballester, A. Leaching of chalcopyrite with ferric ion. Part I: general aspects. *Hydrometallurgy* **93**, 81–87 (2008).
26. Ilin, A. *Microbially-mediated Mineralization Processes in Acid Mine Drainage Systems: Influence on Metal Removal* (University of the Basque Country, 2024).
27. Goh, S. W., Buckley, A. N., Lamb, R. N., Rosenberg, R. A. & Moran, D. The oxidation states of copper and iron in mineral sulfides, and the oxides formed on initial exposure of chalcopyrite and bornite to air. *Geochim. Cosmochim. Acta.* **70**, 2210–2228 (2006).
28. Mikhlin, Y. U. & Tomashevich, Y. E. Pristine and reacted surfaces of pyrrhotite and arsenopyrite as studied by X-ray absorption near-edge structure spectroscopy. *Phys. Chem. Miner.* **32**, 19–27 (2005).
29. Johnson, D. B. & Sánchez-Andrea, I. in *Advances in Microbial Physiology* (ed. Poole, R. K.) Vol. 75 205–231 (Elsevier, 2019).
30. Sánchez-España, J., Ilin, A. & Yusta, I. Metallic copper (Cu[0]) obtained from Cu2+-rich acidic mine waters by two different reduction methods: crystallographic and geochemical aspects. *Minerals* **12**, 322 (2022).
31. Sánchez-España, J. et al. Geochemistry and mineralogy of acid mine drainage in the Iberian Pyrite Belt (Spain, 2004).
32. Johnson, D. B., Hedrich, S. & Pakostova, E. Indirect redox transformations of iron, copper, and chromium catalyzed by extremely acidophilic bacteria. *Front. Microbiol*. **8** (2017).
33. Conejeros, S., Moreira, I. D. P. R., Alemany, P. & Canadell, E. Nature of holes, oxidation states, and hypervalency in covellite (CuS). *Inorg. Chem.* **53**, 12402–12406 (2014).
34. Tornos, F., López-Pamo, E. & Sánchez-España, J. in *Spanish geological frameworks and geosites. An approach to Spanish geological heritage of international relevance* Ch. 4 (eds. Agueda, J., Suárez-Valgrande, J. P. & Salvador, C.) (Instituto Geológico y Minero de España (IGME), 2009).
35. Sánchez-España, F. *Mineralogy and geochemistry of the massive sulphide deposits of the Northern area of the Iberian Pyrite Belt (San Telmo-San Miguel-Peña del Hierro), Huelva, Spain* (University of the Basque Country, 2000).
36. Pinedo Vara, I. *Piritas de Huelva: su Historia, Minería y Aprovechamiento*. (Summa, 1963).
37. Dold, B. Speciation of the most soluble phases in a sequential extraction procedure adapted for geochemical studies of copper sulfide mine waste. *J. Geochem. Exploration* **80**, 55–68 (2003).
38. Poulton, S. W. & Canfield, D. E. Development of a sequential extraction procedure for iron: implications for iron partitioning in continentally derived particulates. *Chem. Geol.* **214**, 209–221 (2005).
39. Diez-Ercilla, M., Falagán, C., Yusta, I. & Sánchez-España, J. Metal mobility and mineral transformations driven by bacterial activity in acidic pit lake sediments: evidence from column experiments and sequential extraction. *J. Soils Sediment.* **19**, 1527–1542 (2019).
40. Parkhurst, D. L. & Appelo, C. a. J. *Description of Input and Examples for PHREEQC Version 3: A Computer Program for Speciation, Batch-Reaction, One-Dimensional Transport, and Inverse Geochemical Calculations*. https://pubs.usgs.gov/publication/tm6A43 (2013).
41. Nordstrom, D. K. & Campbell, K. M. Modeling low-temperature geochemical processes: **7**, 27–68 (2014).
42. Sánchez-España, J. & Diez-Ercilla, M. in *Geochemistry Research Advances* (ed. Stefansson, O.) 31–55 (Nova Science Publishers Inc, 2008).
43. Ball, J. W. & Nordstrom, D. *User's Manual for WATEQ4F, with Revised Thermodynamic Data Base and Text Cases for Calculating Speciation of Major, Trace, and Redox Elements in Natural Waters*. 193, https://doi.org/10.3133/ofr91183 (1991).
44. Scheinost, A. C. et al. ROBL-II at ESRF: a synchrotron toolbox for actinide research. *J. Synchrotron Rad.* **28**, 333–349 (2021).
45. Stöhr, J. *NEXAFS Spectroscopy*. 25 (Springer Berlin Heidelberg, 1992).
46. Reich, T. et al. The Rossendorf Beam Line ROBL—a dedicated experimental station for XAFS measurements of actinides and other radionuclides. *Radiochimica Acta.* **88**, 633–638 (2000).
47. Berger, M. et al. XCOM: Photon Cross Sections Database. NIST Standard Reference Database 8 (2010).
48. Webb, S. M. SIXpack: a graphical user interface for XAS analysis using IFEFFIT. *Phys. Scr.* **2005**, 1011 (2005).
49. Ressler, T. WinXAS: a program for X-ray absorption spectroscopy data analysis under MS-windows. *J. Synchrotron Rad.* **5**, 118–122 (1998).
50. Ankudinov, A. L. & Rehr, J. J. Relativistic calculations of spin-dependent x-ray-absorption spectra. *Phys. Rev. B.* **56**, R1712–R1716 (1997).
51. Ravel, B. & Newville, M. *ATHENA*, *ARTEMIS*, *HEPHAESTUS*: data analysis for X-ray absorption spectroscopy using *IFEFFIT*. *J. Synchrotron Radiat.* **12**, 537–541 (2005).
52. Sorrentino, A. et al. MISTRAL: a transmission soft X-ray microscopy beamline for cryo nano-tomography of biological samples and magnetic domains imaging. *J. Synchrotron Radiat.* **22**, 1112–1117 (2015).
53. Kördel, M. et al. Laboratory water-window x-ray microscopy. *Optica* **7**, 658 (2020).
54. Kremer, J. R., Mastronarde, D. N. & McIntosh, J. R. Computer visualization of three-dimensional image data using IMOD. *J. Struct. Biol.* **116**, 71–76 (1996).
55. Messaoudil, C., Boudier, T., Sorzano, C. O. S. & Marco, S. TomoJ: tomography software for three-dimensional reconstruction in transmission electron microscopy. *BMC Bioinform.* **8**, 288 (2007).
56. Liu, Y. et al. *TXM-Wizard*: a program for advanced data collection and evaluation in full-field transmission X-ray microscopy. *J. Synchrotron Radiat.* **19**, 281–287 (2012).
57. Evans, H. T. The crystal structures of low chalcocite and djurleite. *Z. Kristallographie—Crystalline Mater.* **150**, 299–320 (1979).

Acknowledgements

This study was funded by the Spanish Ministry of Economy, Industry and Competitiveness through the National Research Agency (FEDER funds, grant CGL2016-74984-R) to JSE, IY and AI, and the Basque Government (Consolidated Group IT1678-22) to IY and AI. The authors are grateful for the technical support provided by SGIker (UPV/EHU). We sincerely appreciate the Polymer Research Group from Materials Physics Center (CFM-CSIC) for granting access to the glove box for sample preparation. We acknowledge the European Synchrotron Radiation Facility (ESRF) for provision of beam time under proposal number 84935 and we would like to thank Dr. Nils

Baumann and Joerg Exner for assistance and support in using the beamline BM20 ROBL. Additionally, cryo-TXM experiments were performed at BL09 Mistral beamline at ALBA Synchrotron with the collaboration of ALBA staff. The APC for this manuscript has been partly funded by projects MCIN/AEI/10.13039/501100011033, PID2022-142490OB-C31/AEI/10.13039/501100011033 and CSIC OEP2022.

Author contributions

A.I.M., I.Y., and J.S. conceptualized the study, carried out mineral characterization, and were involved in all aspects of data acquisition, analysis, and interpretation. A.M.A. assisted with electron microscopy. M.I., A.Sch., D.P., A.Sor. assisted with synchrotron experiments, including proposal preparation, data collection, and interpretation. R.O. assisted with cryogenic sample preparation at ALBA. C.G. and I.S. carried out microbial analyses. Z.L., W.H., Y.L., D.A., and K.K. assisted with sequential extraction and porewater analyses. Manuscript writing was led by A.I.M., with substantial input from I.Y. and J.S., and all authors provided feedback that shaped the research and final manuscript.

Competing interests

The authors declare no competing interests.

Additional information

Supplementary information The online version contains supplementary material available at https://doi.org/10.1038/s43247-025-02872-3.

Correspondence and requests for materials should be addressed to Andrey M. Ilin.

Peer review information *Communications Earth & Environment* thanks René H. Lara, Elizabeth Watkin and the other, anonymous, reviewer(s) for their contribution to the peer review of this work. Primary Handling Editors: D'Arcy Meyer-Dombard, Somaparna Ghosh, Carolina Ortiz Guerrero A peer review file is available.

---

[1]Dept. of Geology, University of the Basque Country (UPV/EHU), Barrio Sarriena s/n, Leioa, Spain. [2]Centro de Física de Materiales (CSIC-UPV/EHU), Paseo de Manuel Lardizabal, 5, Donostia, Spain. [3]Servicio de Caracterización de Polímeros (SGIker-UPV/EHU), Avda. Tolosa, 72, Donostia, Spain. [4]Department of Geoscience and Engineering, Delft University of Technology, Stevinweg 1, Delft, The Netherlands. [5]Science and Technology School IE University, Cardenal Zuñiga, 12, Segovia, Spain. [6]The Rossendorf Beamline (BM20), European Synchrotron Radiation Facility (ESRF), 71, avenue des Martyrs, Grenoble, France. [7]Institute of Resource Ecology, Helmholtz-Zentrum Dresden-Rossendorf, Dresden-Rossendorf, Germany. [8]ALBA Synchrotron Light Source, Carrer de la Llum 2-26, Cerdanyola del Vallés, Spain. [9]Department of Geology, Lakehead University, Thunder Bay, ON, Canada. [10]State Key Laboratory of Continental Dynamics, Shaanxi Key Laboratory of Early Life and Environment, Department of Geology, Northwest University, 229 Taibai North Road, Xi'an, P. R. China. [11]Department of Earth and Atmospheric Sciences, University of Alberta, Edmonton, AB, Canada. [12]Planetary Geology and Atmospheres Research Group, Department of Planetary Geology and Habitability, Centro de Astrobiología (CSIC-INTA), Ctra de Torrejón a Ajalvir, km 4, Torrejón de Ardoz, Spain. [13]Present address: Dept. of Geosciences, University of Tuebingen, Schnarrenbergstrasse 94-96, Tuebingen, Germany. ✉e-mail: andrey.ilin@ehu.eus